# Design and test for a new Plasma Analyzer


## Abstract

Measurements of plasma dynamics and diagnostics are essential for understanding the planetary and interplanetary environment and its variability induced by solar forcing (e.g., Space Weather topics). The interest in monitoring the plasma environment is twofold: a scientific objective to deepen our understanding of the Earth's environment and a technological one to understand secondary effects on satellites and other instruments.

The proposed compact Plasma Analyzer for measuring modulations in ionospheric plasma is envisioned to equip instrumentation on satellites in low Earth orbit. One of the most challenging aspects to obtain an instrument with compact size is the development of a single sensor capable sensor capable of measuring either ion energy or direction through different operating modes (*Retarding Potential Analyzer* mode - RPA mode - and *Ion Drift Meter* mode - IDM mode - respectively) .

This technical report aims to outline the sensor features and the test to validate its design.

## Table of Contents

*Abstract*.....2
*1. Introduction*.....4
*2. Sensor design*.....6
*3. Test description*.....7
Mechanical tools.....7
Electrical connection.....8
Signal acquisition.....9
*4. IDM measurements*.....10
*5. RPA measurements*.....13
RPA data validation.....15
*6. Discussion and Conclusion*.....18
*References*.....19

# 1. Introduction

Retarding Potential Analyzers (RPAs) and Ion Drift Meters (IDMs) are instruments devoted to the measurement of thermal ion properties and bulk ion motion. They are typically used on low-Earth-orbit spacecraft. Together, they provide particle velocity and energy, which are key observables for ionospheric dynamics studies.

The RPA (Heelis and Hanson [1998]) is an instrument designed to evaluate the ion energy distribution. It records the ion flux impinging on the sensor by controlling the ion access via a variable potential. A voltage ramp inside the instrument is used to select only particles with energy greater than the voltage step. The instrument outputs an I–V curve that represents the current values generated by the particles reaching the sensor at a specific voltage step. From these data, ion energy can be estimated.

RPAs commonly consist of cylindrical cavities equipped with a series of internal grids biased at different voltages, each serving a specific function. The outermost grid acts as a shield to prevent the internal fields from influencing the external plasma; it could be biased at the spacecraft ground or slightly negative. Moving toward the sensor, inner grids (“retarding grids”) are connected to a circuit that generates a voltage ramp, acting as a voltage bias over a range of values. Consequently, the energy threshold required for particles to reach the detector changes over time. Towards the electrode, another shield grid can be used to protect the sensor from the retarding potential generated by the previous grid. Finally, the nearest grid, called the suppressor grid, is biased to a negative voltage. This grid acts as a barrier to prevent electrons from accessing the collector and to suppress secondary electron emission from the collector.

The IDM (Heelis and Hanson [1998]) is an instrument able to estimate the ion impact angle. It measures the current asymmetry on the detector surface caused by deviations from normal incidence. It is structurally similar to an RPA. Indeed, it features a cylindrical cavity containing a series of grids. All the previously described grids can be used in an IDM. However, it must be noted that the voltage sweeping grid can be omitted, resulting in the loss of the spacecraft-motion ion velocity component but allowing an increase in sampling rate.
Physically, a diaphragm of arbitrary shape selects a beam of ions that impacts the sensor at a specific angle, projecting a “shadow” on the collector. The sensor is divided into four quadrants, each measuring the current independently. The fraction of illuminated area on each quadrant is proportional to the collected current.

From the asymmetries in the current collection, the impact angle can be estimated. The diaphragm shape strongly influences the analysis process and the impact angle calculation. Refer to Heelis and Hanson [1998] for the square diaphragm and Lin et al. [2017] for the circular diaphragm.
Instruments like these, or closely related designs, are widely used in space-plasma studies and fly aboard numerous spacecraft. Some examples include DMSP F7-F18 (Rich and Hairston [1994]), DE-2 (Heelis and Hanson [1980]), C/NOFS (Stoneback and Heelis [2012]), ROCSAT-1/FORMOSAT-1 (Yeh et al. [1999]), ICON (Heelis et al. [2017]), and CSES-01/02 (Liu et al. [2019]).

Based on available instrument specifications, the normal operating ranges can be stated as follows:

energies from 0 eV to approximately 100 eV, and velocities from a few km/s to several tens of km/s.
The uncertainties in velocity measurements depend on the voltage ramp resolution.
Comparing IDM instrumentation across various missions, the values reported in the literature show typical FOV (Field of View ) ranges between 30° and 45° (see Heelis et al. [2017] and Cooke et al. [2003]).
Regarding the FWHM (Full Width at Half Maximum) of the peak obtained by differentiating the current values collected by the RPA, only limited direct information is available in the literature. However, a typical energy range between 0.5 eV and 2.5 eV can be identified; see Heelis et al. [2017], Ogilvie et al. [1995], and Loto'aniu et al. [2022].

In the following sections, we describe the sensor design (Sect. 2); the test details (including the facility and the tools in Sect. 3); IDM mode measurements (Sect. 4); RPA mode measurements (Sect. 5) and finally, discussion and the conclusion (Sect. 6).

## Acronyms

| | |
|---|---|
| **FC** | Faraday Cup |
| **FOV** | Field Of View |
| **FWHM** | Full Width at Half Maximum |
| **IAPS** | Istituto di Astrofisica e Planetologia Spaziali |
| **IDM** | Ion Drift Meter |
| **IEDF** | Ion Energy Distribution Function |
| **INAF** | Istituto Nazionale di Astrofisica |
| **I-V** | Current-Voltage |
| **LEO** | Low Earth Orbit |
| **OML** | Orbital Motion Limited |
| **PA** | Plasma Analyzer |
| **PXI-NI** | Platform for eXtensions for Instrumentation - National Instruments |
| **QFG** | Gaussian Quality Factor |
| **QFS** | Saturation Quality Factor |
| **R** | Reliability |
| **RPA** | Retarding Potential Analyzer |
| **S/C** | Spacecraft |
| **SWIPS** | Solar Wind and Ionospheric Plasma Simulator |
| **UV** | Ultra Violet |

# 2. Sensor design

The single sensor for measurements consists of a Faraday Cup (FC). Its general characteristics are:

- Cylindrical structure made of conductive material (see Figure 1)

  The use of AISI 316 stainless steel is preferred due to its very low residual magnetism and its mechanical resistance to sputtering and heating due to particle impact.

- Presence of insulators

  Steatite is used in engineering models due to its high dielectric properties and good mechanical strength. Once pressed and suitably shaped, it is then baked at over 1300°C. In applications up to 1000°C, it is stable in both its electrical and thermo-mechanical properties. Furthermore, it is resistant to aging and UV rays.

- Presence of grids to filter plasma entry

  The particle selection grids are made of tungsten to offer optimal electrical conductivity and mechanical strength despite the thinness of their wires (in the micrometer range). The mesh, of about hundred micrometers, being much smaller than the Debye length ensures adequate electron obstruction and approximately 80% transparency to ion flow.

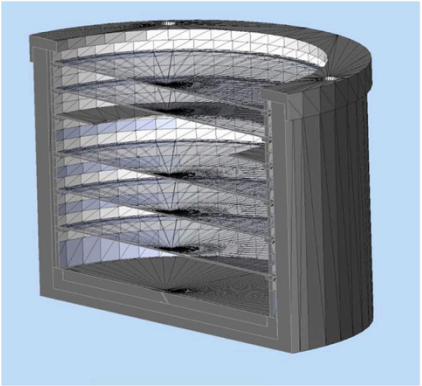

Figure 1: PA sketch. Internal layers represent the particle selection grids

- Collection electrode for measuring plasma currents.

  The ion flux is collected by the circular electrode. Its surface is composed of 4 electrically independent sectors providing independent measures of current (see Figure 2). The analysis of the currents from the various sectors allows the evaluation of the ion beam direction

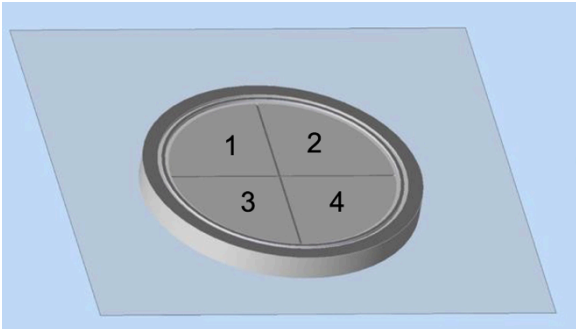


Figure 2: Segmented sensor of PA. The ratios among the different collected currents will allow the computation of the cross-track ion velocity components

In order to test the above-mentioned design features, a prototype of the sensor was built according to the above requirements summarized in Table 1. The FC sensor has been equipped with 5 grids and a diaphragm. All these parts are completely insulated from each other, and from the cylindrical body. Moreover, thanks to separate connection pins (those with blue heat-shrinkable tubing in Figure 3), their polarization can be controlled or adjusted, thus allowing the identification of the best operating setup.
Similarly, the 4 sectors of the collecting electrode were equipped with independent connections to identify and characterize the different currents as the angle of incidence of the particles varies.

| **Parameter** | **Requirement** |
|---|---|
| Target Environment | Low Earth Orbit (LEO) |
| Measurement Type | Thermal ion properties & bulk motion |
| Energy Range | 0 eV to ~20 eV |
| Velocity Range | From few km/s to tens of km/s |
| Angular Coverage (FOV) | 60° (±30° from sensor axis) |
| Energy Resolution | FWHM between 0.5 eV and 3.5 eV |
| Measurement Stability | Reliability > 0.6 within ±30° |

Table 1. Design criteria and material requirements for the Plasma Analyzer development.

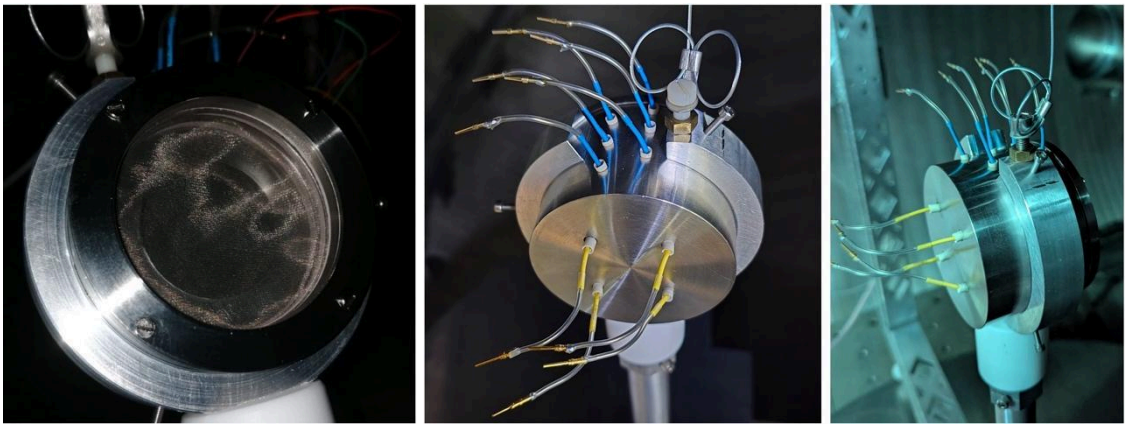

Figure 3: PA sensor prototype. From the left the sensor front side with electron shielding grid, rear side with grids and electrode connections, lateral side.

# 3. Test description

The design of the sensor proposed to integrate RPA and IDM functionalities can be validated through specific test campaigns under conditions representative of the space environment. The INAF-IAPS SWIPS facility (Solar Wind and Ionospheric Plasma Simulator - https://www.iaps.inaf.it/en/facilities/plasma-chamber) provides an experimental environment representative of LEO orbit conditions. The chamber contains a source capable of injecting a plasma with characteristics similar to those of the ionosphere in terms of particle density, velocity and temperature.
Since the facility operates in high vacuum conditions, the entire test has to be conducted remotely. Therefore, specific mechanical setups and electrical connections have to be arranged to obtain complete control of the payload under test.
The specific tools implemented are described in the following section.

## Mechanical tools

The Plasma Analyzer shall operate in space plasma where the ion flux direction can be modulated by geomagnetic structures and by the relevant variation induced by the solar forcing. As a matter of fact, in the Earth's ionosphere the ion collection velocity is mainly due to the S/C motion (i.e. ion flux is opposite to the along-track direction). Nevertheless, plasma drift can occur resulting in different ion beam direction (Fiori et al. [2016]). The experimental setup displayed in Figure 4 has been conceived to verify and characterize the sensor's capability in collecting ion current for different attitudes w.r.t. the ion beam direction. The acquired data from each sector of the electrode provides information relevant to the ion beam direction, thus they are used to check the sensor design when operating as a Ion Drift Meter.

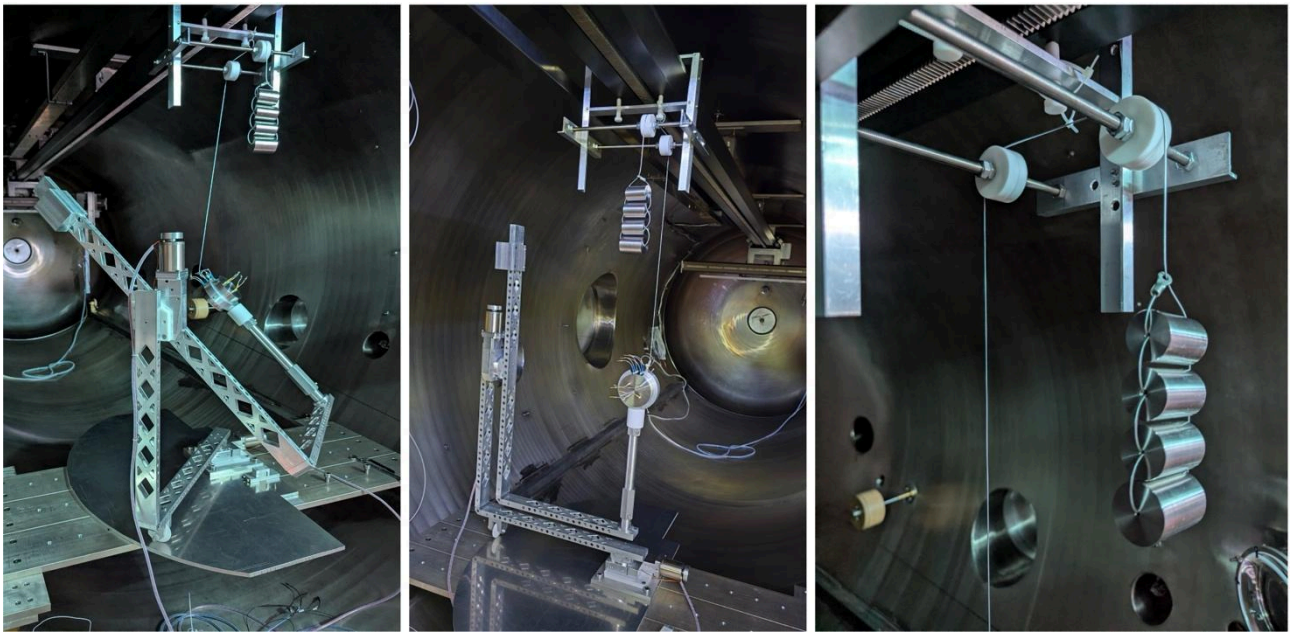

Figure 4: Mechanical support able to rotate the sensor to simulate various attitudes w.r.t plasma beam direction.

The mechanical rotating stage is made of a double L-shaped Aluminium supports equipped with step motors able to operate in high vacuum. In order to avoid an overload on the motors (with significant loss of position accuracy), a counterweight system has been built.
As shown in Figure 4 (right panel), a mass equivalent to the weight of the sensor is connected to the drive via a steel cable and PTFE pulleys are arranged to balance the weight of the sensor in each rotation.

## Electrical connection

The sensor is equipped with independent connections to provide different polarization states of the inner elements (grids and diaphragm) and to acquire the signals from the four sectors of the electrode. In addition, a direct connection to the sensor body is available to enable the control (or possible change) of its floating potential.
All these signals pass through flange-mounted connectors to reach control units outside the chamber, as shown in Figure 5.

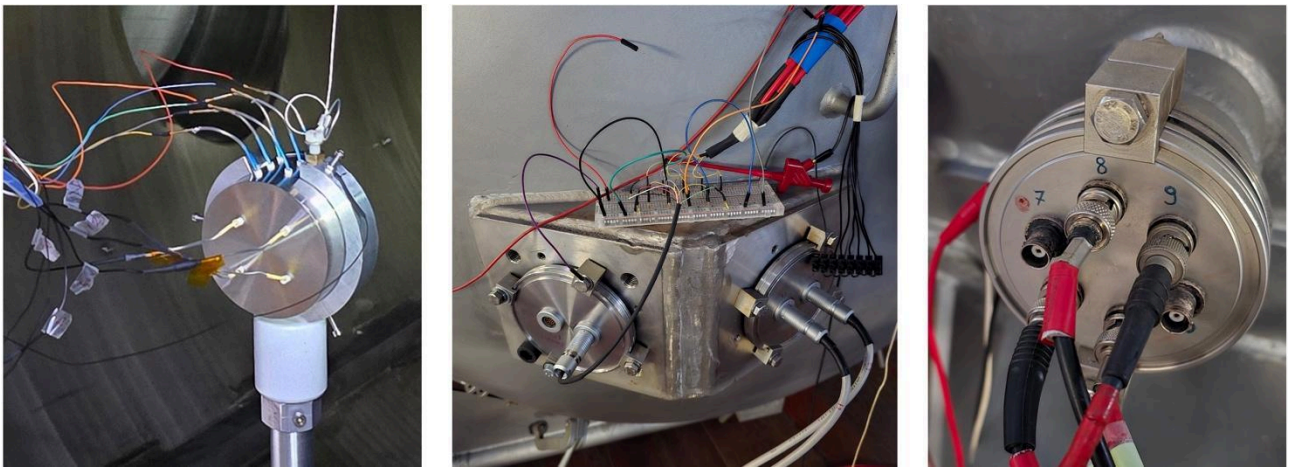


Figure 5: Electric connection. Left: sensor connection. Center: the flange with connectors relevant to grids and movimentation. Right: the flange of the four electrode sectors.

To easily manage the connections between the various elements and the ground references, a board with movable pins was inserted. This allowed us to test different bias configurations without having to vent the high-vacuum experimental environment to act directly on the sensor.

## Signal acquisition

The experimental control unit consists of several elements. The central unit is the facility controller (NI-PXI system), which also manages plasma injection and the diagnostics system.
The experimental tests described in this paper require instrumentation capable of separately acquiring four small-amplitude current signals (order of nA) in quasi-static mode (IDM mode) as well as rapidly modulated signals (order of 100 ms for the RPA mode). For these purposes, a multiplexer (HP 3488A) and an electrometer (Keithley 619A with pA resolution) were respectively used to select and monitor the currents from the electrode sectors.
In particular, during the IDM mode measurements, each electrode sector was manually selected and the ion currents were visually acquired in order to evaluate possible time variations, if any. On the contrary, during the RPA mode the current values were automatically acquired by a specific LabVIEW tool prepared for this test campaign (see Fig.6)

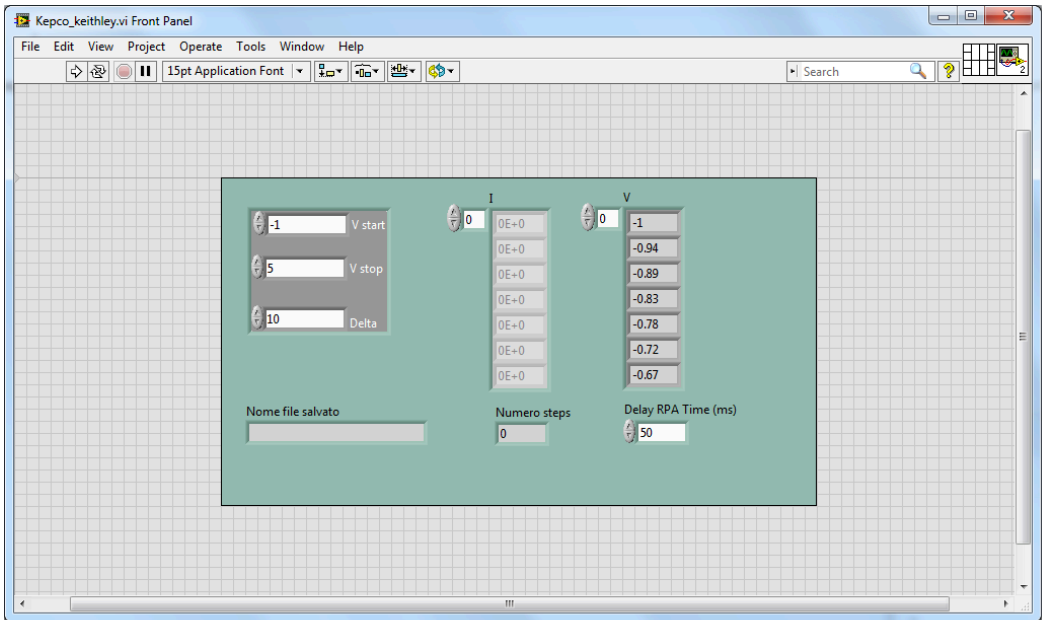


Figure 6. Control panel of the LabVIEW SW developed to control the voltage ramp and acquire the I-V characteristic curve of the sensor.

# 4. IDM measurements

The aim of the Ion Drift Meter measurement is to evaluate the plasma dynamics through an accurate measurement of the velocity components. For this purpose, it is necessary that the measurement of the currents collected by the individual sectors of the electrode allows the angle of incidence of the plasma beam to be derived. To verify this possibility, geometrical considerations have been used to identify the relationships linking the angle of incidence to the collected currents.

In this section we present a summary of the basic geometry needed to perform the simulation, and its comparison with experimental data

As a first approximation, the current measured in each quadrant is considered proportional to its illuminated area (i.e. the surface reached by an ion collimated beam): $A_i/A_{tot} = I_i/I_{tot}$, where $A_i$ and $I_i$ are the illuminated area and measured current of the $i$-th quadrant, respectively, while $A_{tot}$ and $I_{tot}$ represent the total values. The instrument outputs individual quadrant currents ($I_i$), which are summed to obtain $I_{tot}$.
To determine $A_i$, the total illuminated area $A_{tot}$ is required. Since the projected shadow maintains the circular shape of the diaphragm (of radius Rd), we can define $A_{tot} = \pi R_d^2$, leading to $A_i = (I_i \pi R_d^2)/I_{tot}$ .
The impact angle can be extracted once the quadrant areas are known. As shown in Figure 7 (left panel), these areas ($S_1$ to $S_4$) represent the intersections between the illuminated region (yellow) and the four sensor quadrants. By vertically summing quadrants $S_2$ and $S_3$, we obtain the circular segment $A_{seg}$ (highlighted in red). Geometrically, $A_{seg}$ is the difference between the circular sector ($A_{sec} = R_d^2\theta/2$, purple) and the subtended triangle ($A_{tri} = R_d^2 sin(\theta)/2$, green).
To isolate the angular dependence, the formula is rearranged as follows:

$$A_{seg} = R_d^2 \frac{[\theta - sin(\theta)]}{2} \quad \Rightarrow \quad f(\theta) = \theta - sin(\theta) = 2\frac{A_{seg}}{R_d^2}$$

Since this is a transcendental equation, $\theta$ is solved numerically via iterative minimization using the Halley method (Scavo and Thoo [1995]). Once $\theta$ is determined, the distance $d$ between the vertical diameters of the illuminated area and the sensor is calculated through trigonometric relations.
As illustrated in the right panel of Figure 7, $d$ is related to the impact angle $\alpha$ and the instrument depth $D$. Thus, $\alpha$ can be calculated as:

$$d = R_d cos\left(\frac{\theta}{2}\right), \qquad \alpha = arctan\left(\frac{d}{D}\right)$$

These results rely on the assumed proportionality between collected current and illuminated area. However, this approximation may vary depending on the instrument's geometry. To test these limits, we simulated the diaphragm's projection onto the sensor as a function of the inclination angle. The results indicate that the approximation is valid for $\alpha \in [-30^\circ, +30^\circ]$. Beyond this range, the measurements are influenced by additional phenomena and deviate from analytical predictions (Fisher [2016], Nicolle [2022] e Trottemberg [2025]).

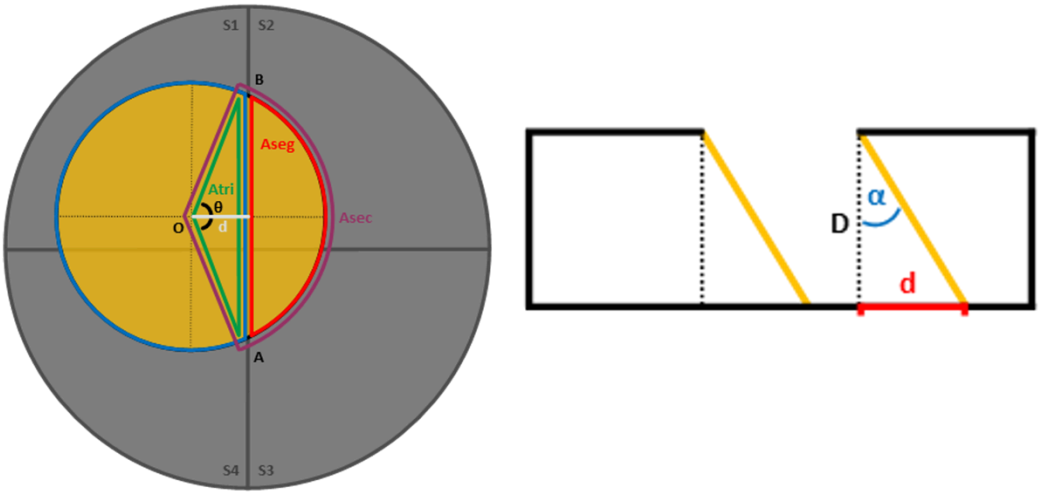


Figure 7. Left panel: Top view of the sensor (grey) and the illuminated area (yellow). Highlighted regions used for analysis include the circular segment ($A_{seg}$, red), the circular sector ($A_{sec}$, purple), and the subtended triangle ($A_{tri}$, green). The central angle θ and the displacement $d$ between the sensor and illuminated area diameters are also shown.
Right panel: Vertical cross-section illustrating the relationship between distance $d$, instrument depth $D$, and impact angle α. The diaphragm projection is highlighted in yellow

The above geometric relationships were used to simulate the amplitude of the signals for various angles (see figure 8).

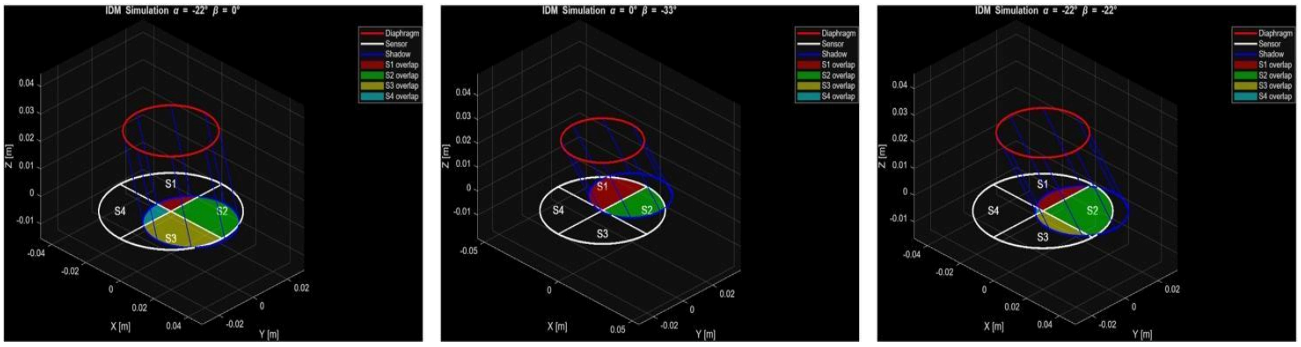


Fig. 8. Simulation of the ion current collected by the electrode sectors for different beam angles.

The values obtained from the simulation were compared with those measured with the same sensor angles. Figure 9 shows the comparison results within amplitudes of +/- 30° revealing a very high correlation between simulation and measurement.

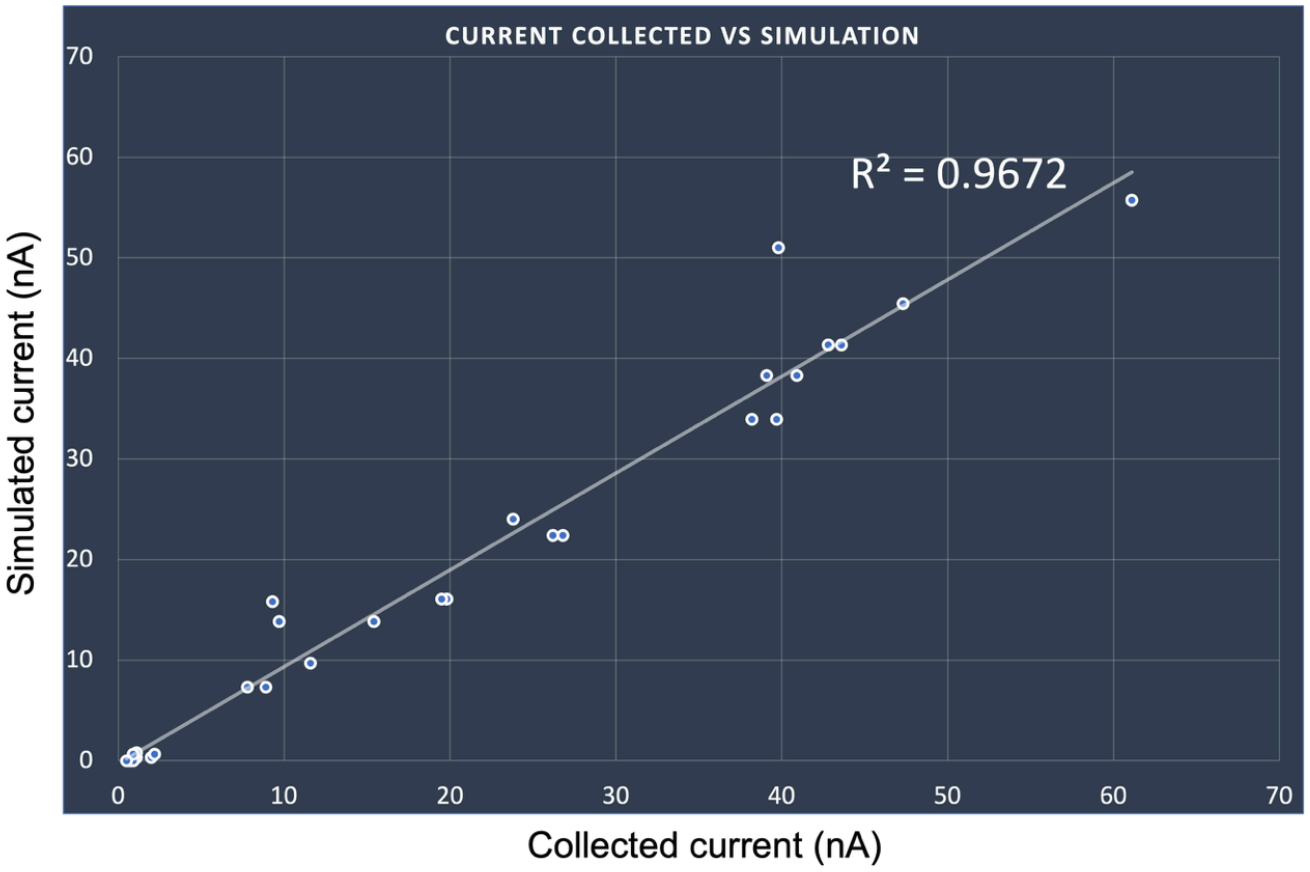


Fig. 9. Squared Pearson correlation coefficient between collected and simulated current for different beam angles ($R^2$=0.9672).

# 5. RPA measurements

The RPA measurement aims to determine the energy of the ion flux in the space plasma.
As already explained in the introduction, the geometry of the sensor and the polarization of the conductive parts must be carefully evaluated for the measurement to be reliable. In particular, the sensor geometry must ensure adequate current collection (i.e., a possibly large aperture diameter) while avoiding bending of the thin grids. Similarly, the internal cavity clearances must be such as to avoid distortion fields of the ion flow, while maintaining compact dimensions. Once the structural needs have been ensured, the correct polarization setting of the internal elements can be identified directly by acting on the connections described in the Test Description section.
However, the RPA measurement cannot be considered separate from that of the IDM since in space we cannot consider the ion flow as coming only in the along-track direction. Therefore, even in RPA mode, the needs and the limits set out in section 4 must be considered to adequately interpret whether the obtained characteristic curve can provide qualitatively reliable information.

In Figure 10, we observe a characteristic curve obtained with a beam parallel to the sensor axis, i.e., in the absence of drift. Under these conditions, the observed signal is extremely clean, and even small features can be observed (e.g., the charge-exchange population at about 2 eV), thus confirming the correct design of the sensor.

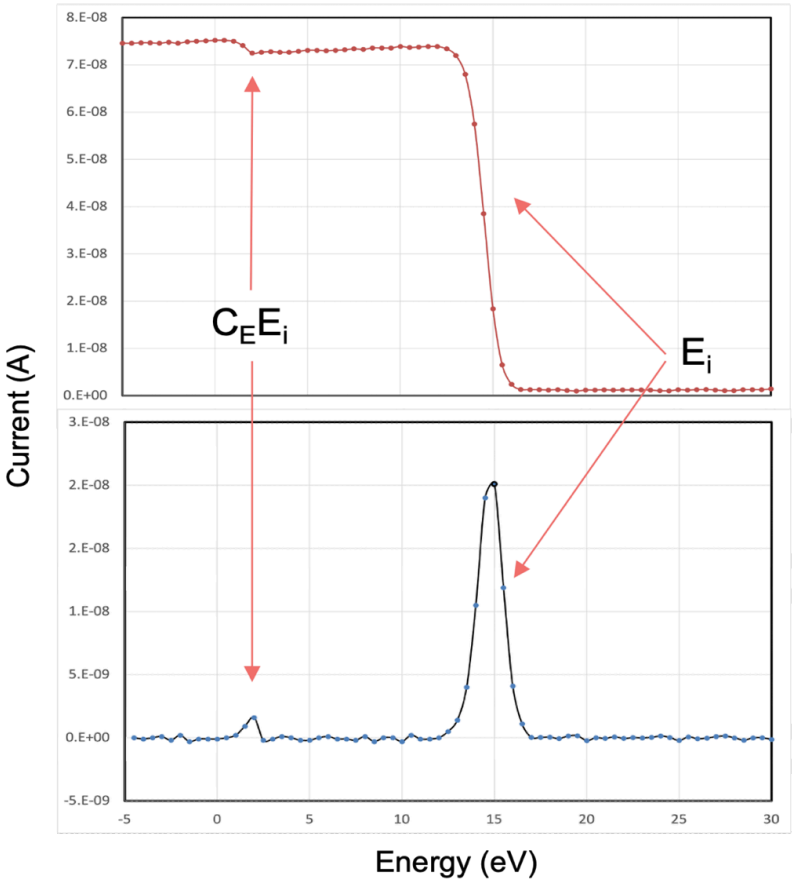


Figure 10. Characteristic I-V curve of the sensor in RPA mode (upper panel) and the first derivative for the energy peak detection. Main variation and the relevant peak

However, in space the ion flux may have a drift velocity that alters the energy (along-track drift component), or the angle of incidence into the sensor (cross-track component). For this reason, in this instrument characterization test, we simulated both of the above-mentioned unfavorable conditions for plasma energy measurement.
Figure 11 shows the different I-V curves obtained for ion energies varying in a very large range. This wide range was designed to validate the instrument under extreme conditions. It is worth noticing that , in ionospheric space, along-track velocity variations of less than 20% are expected.

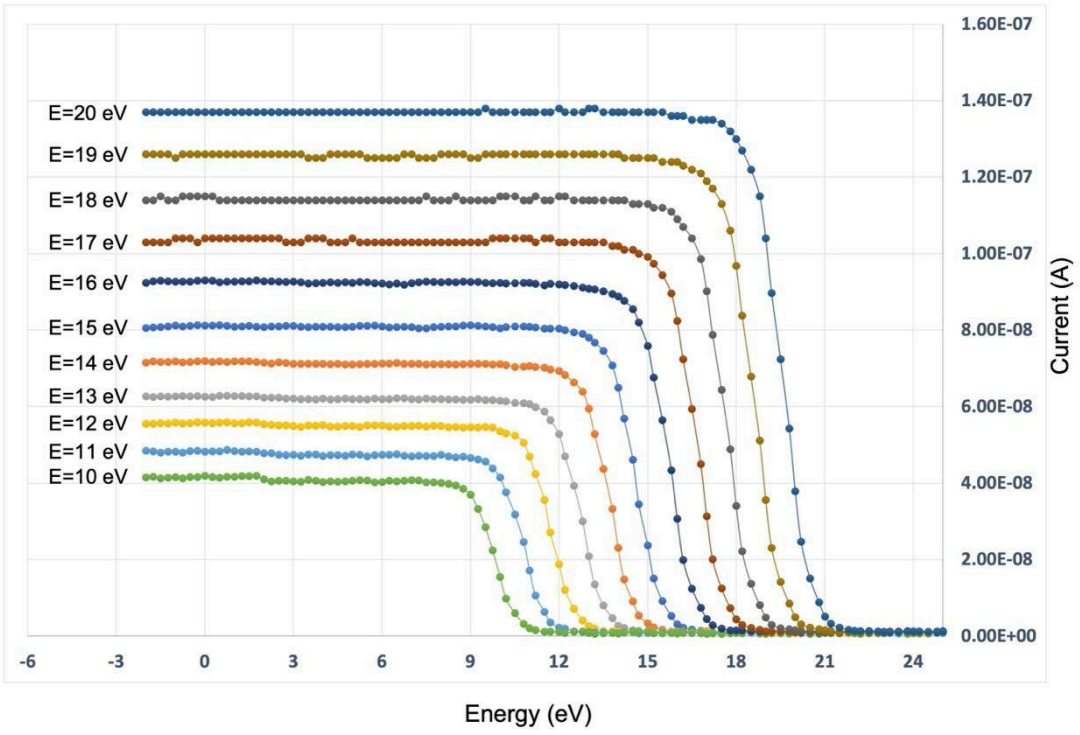


Figure 11. Characteristic curve I-V of the sensor in RPA mode relevant to different ion energies set by the plasma source.

All I-V curves between 10 and 20 eV show a regular trend consistent with the beam energy. The only significant difference is in the value of the saturation current (i.e., the left side of the curve), which, as known from the OML relations, must be linearly proportional to the impact velocity of the incident ions on the electrode.

Figure 12 shows the variations on the characteristic curve induced by the cross-track component. In this case, a clear deformation of the curves is observed as the angle of incidence increases.
It is therefore necessary to define measurement quality and reliability criteria that take into account the shape of the characteristic curve.
In the following section, parameters have been identified to determine the quality of the measurement subject to the exceeding of appropriate threshold values.

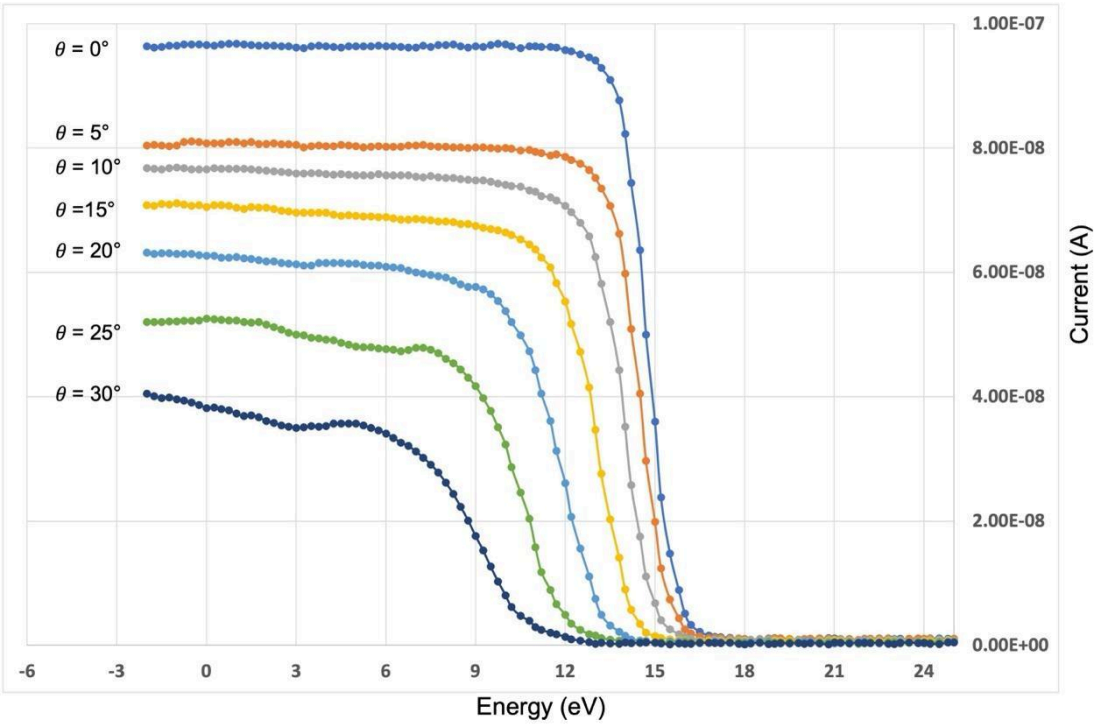


Figure 12. Characteristic I-V curve of the sensor in RPA mode relevant to different ion beam angle w.r.t. the sensor's axis.

## RPA data validation

This section presents the RPA validation analysis, detailing the set of calculations performed to verify the instrument's performance. The analysis is structured as a multistage process: data pre-processing and derivative peak position estimation, saturation region analysis (saturation linear fit), gaussian shape analysis (global gaussian fit), and Quality Factor/Reliability estimation.
Calculations were performed in MATLAB. It should be noted that the study was conducted by simultaneously varying the beam energy and the instrument tilt angle. This approach was chosen to identify and highlight potential issues arising under specific operating conditions.

**Pre-Processing and Peak Position Identification**

The derivative of the I–V curve is proportional to the Ion Energy Distribution Function (IEDF). Derivatives were computed using the *gradient()* function, and the resulting data were fitted with the *fit()* function using a Gaussian distribution ('*gauss1*'). From this analysis, the Gaussian mean $V_0$ and variance σ were extracted, providing crucial information regarding the peak position and its associated uncertainty.
A Gaussian distribution was utilized because it accurately models the energy distribution of a mono-energetic particle beam (Caldarelli et al. [2023]) under the measurement conditions of a plasma chamber.
The top two panels of Figure 12 report the identified peak positions $V_0$ with their uncertainty $\pm\sigma$.
It is evident that increasing the energy shifts the peak position without altering the Gaussian characteristics. Conversely, in the tilt angle case, σ increases with the angle. Consequently, the instrument appears to lose precision when particles arrive at a large angle relative to the detector normal. Furthermore, a shift toward lower energies is observed as the tilt angle increases. This

shifting phenomenon was already studied by Nicolle et al. [2022]. Furthermore, correction algorithms have been developed to re-center the data to the expected values.

**Saturation Region Analysis**

Following peak identification, a deeper analysis of the instrument's performance was conducted by applying a linear fit to the saturation region of the I–V curve (the low bias potential zone).

Theoretically, the I–V curve should resemble a complementary error function, presenting a constant plateau. However, some spurious interactions can introduce a decreasing linear trend instead of a constant saturation value.

As reported in Heelis and Hanson [1998] and Fisher et al. [2016], the interaction between ions and the plasma sheath generated by the spacecraft can modify the measured ion characteristics. Sheath interactions can deflect particle trajectories, thereby influencing the number of collected ions. Moreover, considering the results of Nicolle et al. [2022], it appears that the non-constant linear trend observed in the saturation region may also originate from secondary particles emitted by primary particles that are not collected by the sensor because they impact outside its sensitive area. Finally, Trottenberg et al. [2025] demonstrated that the alignment of the instrument grids can lead to multiple distortions of the I–V curves, including the inclination of the saturation region.

It is clear that the saturation slope is a crucial parameter for understanding the instrument's behavior. By fitting the initial part of the curve and extracting its slope, we can quantify the extent of these interferences.

The second row of Figure 12 shows the extracted slopes for each measurement configuration. The slopes approach zero as energy increases. Conversely, the slopes degrade as the tilt angle increases. The data points are visualized using a color scale from red to green, representing the Saturation Quality Factor (QFS). This factor ranges from 0 to 1, where 0 corresponds to the maximum saturation slope and 1 to the minimum.

As shown in Figure 12, the QFS remains high as energy increases but degrades with the angle. In conclusion, all the previously presented problems are negligible below 15°, minimal between 15° and $30°$, and becomes a disabling factor above $30°$.

**Gaussian Shape Analysis**

Another critical parameter is the Gaussian shape of the I–V data derivative. To ensure the instrument is operating correctly, deviations from the Gaussian distribution must be quantified, since the expected distribution of a mono-energetic ion beam should be Gaussian (Caldarelli et al. [2023]).

To analyze the derivative shape, a Gaussian fit is applied to the data, and the deviations of the data points from the fitted function are recorded. The third row of Figure 12 shows the summed errors to represent the global fit error, highlighting the deviation of the data from Gaussian behavior.

Similarly, a parameter was defined to quantify measurement quality based on the fit error: the higher the error, the lower the parameter. This parameter, termed the Gaussian Quality Factor (QFG), is computed by normalizing the fit-error scale and assigning the lowest quality factor to the largest error and the highest quality factor to the smallest.

The error remains approximately constant, with only a slight increasing trend as the energy increases. Furthermore, the error stays limited at small angles, becomes progressively more significant as the tilt angle increases, and ultimately reaches the worst instrument response at $40^{\circ}$.

**Reliability**

Finally, a global parameter summarizing the overall measurement reliability was defined. This "Reliability" (R) is calculated as the weighted average of the two previously introduced quality factors. It should be noted that the optimal weighting of these factors is still under study ; however, they are currently weighted according to the number of data points used in the fits.
The Reliability as a function of energy and tilt angle is reported in the fourth row of Figure 12. In the energy-varying case, reliability remains consistently around 0.8. In contrast, in the tilt angle case, reliability stays at 0.8 only below 15°, drops to approximately 0.6 between 15° and 30°, and subsequently decreases toward 0.

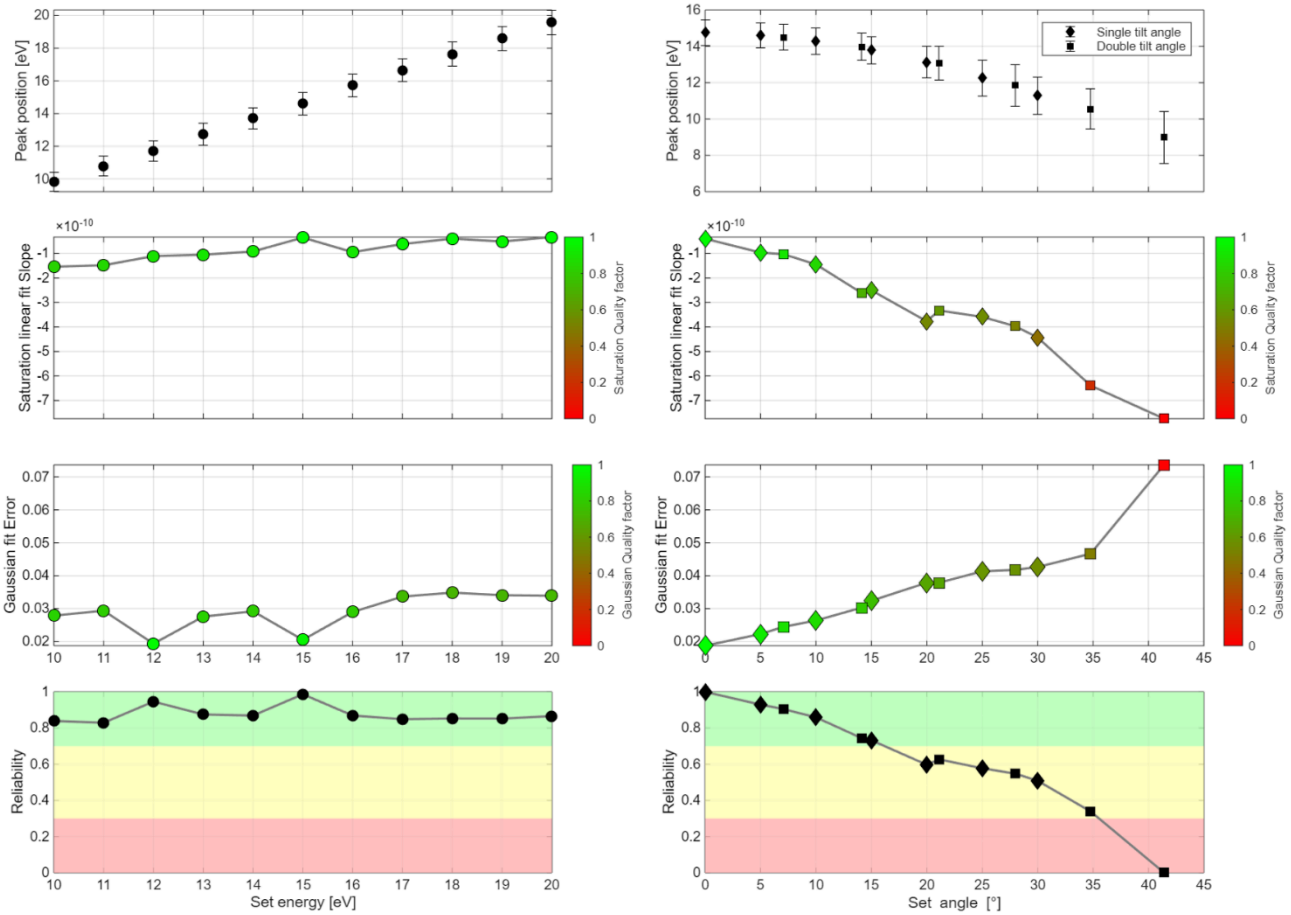


Figure 12. Instrument validation graphs. The two columns represent two different sets of measurements: beam energy (left) and instrument tilt angle (right).
The **first row** shows the detected peak position using a Gaussian fit on the derivative of the I-V curve, with the associated error (± σ). For the tilt angle case, data are represented by **diamonds** for single-axis tilts and **squares** for dual-axis tilts.
The **second row** reports the slope of the linear fit in the saturation region, with the color scale indicating the Saturation Quality Factor (QFS).
The **third row** reports the gaussian fit error over the data derivative, with the color scale indicating the Gaussian Quality Factor (QFG).
The **fourth row** reports the Reliability (R), calculated from the weighted average of the two quality factors.

# 6. Discussion and Conclusion

This technical note describes the testing and validation process of an innovative instrument that combines energy and direction measurements of the ionic component of space plasma in LEO orbit in a single sensor.
For this purpose, wide-ranging activities were required, including mechanical, electronic and software developments, all essential to ensure a correct testing procedure and allow a correct analysis of the obtained data.

IDM mode

- Sensor shape has been conceived to allow the detection of plasma beam direction in a wide angle corresponding to a FOV of about 60° ($\pm$ 30° w.r.t sensor axis) to evaluate the cross-track velocity components.
- Various simulations have been computed to outline the expected areas reached by the plasma beam for different angles.
- Plasma currents collected by each sector of the anode have been compared with the corresponding simulations to check the accordance between the attitude and the measurements.

Results confirm that the beam angle and the cross-track components can be retrieved with high reliability in the range [-30°; +30°].

RPA mode:

- the instrument must allow the acquisition of a correct characteristic curve in a wide range of energy and direction of the incident beam
- the cross-track component of the velocity can significantly alter the characteristic curve and the consequent failure of the measurement
- To identify the quality or failure criteria of the measurement, the trends of the exponential and saturation regions of the curves and associated parameters were studied.

The RPA mode also demonstrates good measurement quality over a wide range of along-track variation, while the cross-track component confirms the reliability interval already identified for the IDM mode.
It should be noted that the aforementioned reliability interval within [-30°; 30°] represents an excellent result in the context of current and past space-based measurements. Furthermore, this range is fully compatible with what is expected in LEO orbit.

# References

J. K. Burchill and D. J. Knudsen. Swarm thermal ion imager measurement performance. Earth, planets and space, 74(1):181, 2022.

A. Caldarelli, F. Filleul, R. W. Boswell, C. Charles, N. J. Rattenbury, J. E. Cater; Data processing techniques for ion and electron-energy distribution functions. *Phys. Plasmas* 1 April 2023; 30 (4): 040501. https://doi.org/10.1063/5.0133840

D. L. Cooke, C. W. Turnbull, C. Roth, A. Morgan, and R. Redus. Ion drift-meter status and calibration. First champ mission results for gravity, magnetic and atmospheric studies, pages 212–219, 2003.

Fiori, R.A.D., Koustov, A.V., Boteler, D.H. et al. Calibration and assessment of Swarm ion drift measurements using a comparison with a statistical convection model. Earth Planet Sp 68, 100 (2016). https://doi.org/10.1186/s40623-016-0472-7

L. E. Fisher, K. A. Lynch, P. A. Fernandes, T. A. Bekkeng, J. Moen, M. Zettergren, R. J. Miceli, S. Powell, M. R. Lessard, P. Horak; Including sheath effects in the interpretation of planar retarding potential analyzer's low-energy ion data. *Rev. Sci. Instrum.* 1 April 2016; 87 (4): 043504. https://doi.org/10.1063/1.4944416

R. Heelis and W. Hanson. Measurements of thermal ion drift velocity and temperature using planar sensors. Measurement techniques in space plasmas: particles, 102:61–71, 1998.

R. Heelis, R. Stoneback, M. Perdue, M. Depew, W. Morgan, M. Mankey, C. Lippincott, L. Harmon, and B. Holt. Ion velocity measurements for the ionospheric connections explorer. Space Science Reviews, 212(1):615–629, 2017.

R. A. Heelis and W. B. Hanson. The ion drift meter for dynamics explorer. Space Science Instrumentation, 5: 515–522, 1980.

D. Knudsen, J. Burchill, S. Buchert, A. Eriksson, R. Gill, J.-E. Wahlund, L. Åhlén, M. Smith, and B. Moffat. Thermal ion imagers and langmuir probes in the swarm electric field instruments. Journal of Geophysical Research: Space Physics, 122(2):2655–2673, 2017.

Z.-W. Lin, C.-K. Chao, J.-Y. Liu, C.-M. Huang, Y.-H. Chu, C.-L. Su, Y.-C. Mao, and Y.-S. Chang. Advanced ionospheric probe scientific mission onboard formosat-5 satellite. Terrestrial, Atmospheric & Oceanic Sciences, 28(2), 2017.

C. Liu, Y. Guan, X. Zheng, A. Zhang, P. Diego, and Y. Sun. The technology of space plasma in-situ measurement on the china seismo-electromagnetic satellite. Science China Technological Sciences, 62(5):829–838, 2019.

P. T. Loto'aniu, K. Romich, W. Rowland, S. Codrescu, D. Biesecker, J. Johnson, H. J. Singer, A. Szabo, and M. Stevens. Validation of the dscovr spacecraft mission space weather solar wind products. Space Weather, 20 (10):e2022SW003085, 2022.

L. Nicolle , P. Sarrailh, L. Garrigues, S. Hess and M. Villemant (2022) Modeling of a retarding potential analyzer and comparison with Express-A in-flight measurements. Front. Phys. 10:862945. doi: 10.3389/fphy.2022.862945

K. Ogilvie, D. Chornay, R. Fritzenreiter, F. Hunsaker, J. Keller, J. Lobell, G. Miller, J. Scudder, E. Sittler Jr, R. Torbert, et al. Swe, a comprehensive plasma instrument for the wind spacecraft. Space Science Reviews, 71 (1):55–77, 1995.

F. Rich and M. Hairston. DMSP SSIES Instrument Description and User Guide, 1994. Technical documentation for the Special Sensor Ions, Electrons, and Scintillation instrument.

Scavo, Thomas R. and John B. Thoo. “On the Geometry of Halley's Method.” *American Mathematical Monthly* 102 (1995): 417-426.

R. A. Stoneback and R. A. Heelis. Calibration and validation of the cindi instruments on c/nofs. Radio Science, 47:RS0L06, 2012.

T. Trottenberg, F. Bansemer, M. Hesse, H. Kersten, J. Laube, V. Schneider, B. Schuster, L. Seimetz, R. F. Wimmer-Schweingruber; The role of grid geometry and relative orientation in the performance of a retarding potential analyzer. *AIP Advances* 1 March 2025; 15 (3): 035030. https://doi.org/10.1063/5.0250806

H.-C. Yeh et al. Scientific mission of the ipei payload onboard rocsat-1. Terrestrial, Atmospheric and Oceanic
Sciences, (1):19–42, 1999.